GEOPHYSICS, VOL. 72, NO. 4 (JULY-AUGUST 2007); P. H43–H53, 10 FIGS.
10.1190/1.2732555

Efficient FDTD algorithm for plane-wave simulation for vertically heterogeneous attenuative media

Arash JafarGandomi[1] and Hiroshi Takenaka[1]

ABSTRACT

We propose an efficient algorithm for modeling seismic plane-wave propagation in vertically heterogeneous viscoelastic media using a finite-difference time-domain (FDTD) technique. In the algorithm, the wave equation is rewritten for plane waves by applying a Radon transform to the 2D general wave equation. Arbitrary values of the quality factor for P- and S-waves (Q_P and Q_S) are incorporated into the wave equation via a generalized Zener body rheological model. An FDTD staggered-grid technique is used to numerically solve the derived plane-wave equations. The scheme uses a 1D grid that reduces computation time and memory requirements significantly more than corresponding 2D or 3D computations. Comparing the finite-difference solutions to their corresponding analytical results, we find that the methods are sufficiently accurate. The proposed algorithm is able to calculate synthetic waveforms efficiently and represent viscoelastic attenuation even in very attenuative media. The technique is then used to estimate the plane-wave responses of a sedimentary system to normal and inclined incident waves in the Kanto area of Japan via synthetic vertical seismic profiles.

INTRODUCTION

For many cases in exploration seismology, plane waves are considered an effective tool. Plane waves can be obtained by decomposition of point-source seismic records to show the corresponding plane-wave reflection response (Tygel and Hubral, 1985; Dietrich, 1990). Plane waves are often used in seismic forward modeling, such as amplitude variation with offset (AVO) analysis, migration studies, reflection/transmission behavior of seismic waves (e.g., Pai, 1988; Mosher et al., 1996; Ursin and Stovas, 2002; Liu et al., 2004; Shan and Biondi, 2004), and inverse modeling of observed, oblique-incidence seismic data (Müller. 1971; Treitel et al., 1982; Kormendi and Dietrich, 1991). The analysis of vertical seismic profiles (VSPs) for mapping between time and depth can be done effectively by calculating synthetic plane-wave records (e.g., Aminzadeh and Mendel, 1985).

It is common in seismic data processing to generate synthetic waveforms for several primary velocity and attenuation models to find the most appropriate one for better imaging of subsurface structure and further processing and interpretation steps. For this purpose, a large number of simulations for many models are required. Because they are very time consuming, a quick and accurate algorithm for generating synthetic waveforms is needed. In this paper we propose an algorithm that uses a finite-difference time-domain (FDTD) technique to solve plane-wave equations and generates synthetic waveforms for vertically heterogeneous attenuative media. To configure the finite-difference (FD) scheme, the algorithm uses a 1D staggered grid. This grid is used by Tanaka and Takenaka (2005) to calculate plane-wave responses of 1D, perfectly elastic media. Because of the relatively small number of introduced grid points compared to 2D and 3D schemes, the 1D scheme is very efficient. The responses of horizontally layered media can be calculated by semianalytical methods such as the propagator matrix method. However, for velocity gradients or randomly heterogeneous structures, use of numerical techniques such as the FD method is mandatory (Fraiser, 1970).

Real earth media are attenuative, so it is necessary to allow for attenuation and dispersion effects of the media on seismic waves. These effects are often quantified by the quality factor Q. Understanding Q is very essential for prospecting subsurface structures and especially oil exploration (e.g., Klimentos, 1995; Dasgupta and Clark, 1998). Klimentos (1995) shows that attenuation of P- and S-waves can be used to distinguish gas from oil and water. The influence of attenuation on the amplitudes of reflected waves may cause misinterpretations in AVO or VSP analysis (Blangy, 1994).

Peer-reviewed code related to this article can be found at software seg.org/2007/~~0004~~. 0005
Manuscript received by the Editor August 10, 2006; revised manuscript received December 26, 2006; published online May 23, 2007; corrected version published online July 3, 2007.
[1]Kyushu University, Department of Earth and Planetary Sciences, Fukuoka, Japan E-mail: gandomi@geo.kyushu-u.ac.jp; takenaka@geo.kyushu-u.ac.jp

Day and Minster (1984) made the first attempt to incorporate anelasticity into a 2D time-domain model by applying the Padé approximation method. Emmerich and Korn (1987), however, find this method inefficient. They suggest an approach based on a generalized Maxwell body, developing a 2D FD algorithm for scalar wave propagation. By using memory variables in the time domain (Carcione et al., 1988a, b; Robertsson et al., 1994; Blanch et al., 1995; Moczo et al., 1997), FD computations have become more suitable for seismic wave simulation in realistic media. In this paper, we apply the memory variable technique to incorporate attenuation into the FD computations for a plane-wave problem.

In the following sections, after a quick review of the viscoelastic wave modeling formulations, we derive the plane-wave equations for vertically heterogeneous media. Then the plane-wave equations are solved numerically by the staggered-grid FD method. Subsequently, we confirm the accuracy of FDTD simulations through numerical tests and then apply the technique to generate a synthetic VSP.

CONSTITUTIVE VISCOELASTIC RELATIONS

In this section, we describe a theoretical anelastic model based on viscoelastic theory, a phenomenological way to represent combined elastic and viscous behaviors of materials.

Attenuation model

In the viscoelastic media, the strain at any time step depends on strain at the previous steps. The relation between present strain and previous ones can be explained in a simple form by the fading-memory theory (Christensen, 1982). According to the fading-memory hypothesis, the current value of strain depends more strongly upon recent strain history than distant history.

Distribution of relaxation mechanisms of rheological models in generalized form can be used to obtain a nearly constant (Liu et al., 1976; Carcione, 2001) or any arbitrary frequency-dependent (Asvadorov et al., 2004) quality factor Q over the seismic frequency range of interest. Emmerich and Korn (1987) show that a generalized Maxwell body can represent viscoelastic behavior of earth materials correctly. Carcione (1988a, b) uses a parallel connection of several standard linear solids (Zener bodies) to develop a theory of a generalized Zener body (GZB). Moczo and Kristek (2005) prove that the resulting relaxation functions of generalized Maxwell and Zener models are equivalent.

In this paper, a GZB with the following relaxation function (Carcione, 2001) is used:

$$\psi(t) = M_R\left[1 - \frac{1}{L}\sum_{l=1}^{L}\left(1 - \frac{\tau_\varepsilon^l}{\tau_\sigma^l}\right)e^{-t/\tau_\sigma^l}\right]H(t), \qquad (1)$$

where t is time; τ_σ^l and τ_ε^l are stress and strain relaxation times of the lth Zener body, respectively; M_R is the relaxed modulus (the value of the relaxation function at the zero frequency or infinite time); L is the number of relaxations; and $H(t)$ is the Heaviside function. Note that equation 1 correctly incorporates the $1/L$ factor in the relaxation function, which had not been considered before Carcione (2001) (e.g., Robertsson et al., 1994; Blanch et al., 1995).

Q is defined as (O'Connell and Budiansky, 1978)

$$Q(\omega) = \frac{\Re[\psi(\omega)]}{\Im[\psi(\omega)]}, \qquad (2)$$

where ω is angular frequency, $\psi(\omega)$ is the relaxation function in the frequency domain, and $\Re[.]$ and $\Im[.]$ indicate real and imaginary parts of the argument, respectively. For an array of Zener bodies (GZB),

$$Q(\omega) = \frac{\displaystyle\sum_{l=1}^{L}\frac{1+\omega^2\tau_\varepsilon^l\tau_\sigma^l}{1+\omega^2(\tau_\sigma^l)^2}}{\displaystyle\sum_{l=1}^{L}\frac{\omega(\tau_\varepsilon^l-\tau_\sigma^l)}{1+\omega^2(\tau_\sigma^l)^2}}. \qquad (3)$$

In equation 3, the values of the stress and strain relaxation times (τ_ε and τ_σ) must be optimized to reach the target quality factor $Q_0(\omega)$. They can be estimated by minimizing S in a least-squares sense:

$$S = \int [Q_0^{-1}(\omega) - Q^{-1}(\omega)]^2 d\omega. \qquad (4)$$

This optimization must be performed for the desired Q for both P- and S-waves (Q_P, Q_S), which yields τ_ε^{Pl} and τ_ε^{Sl}. The same stress relaxation times τ_σ^l can be used for both wave types (Blanch et al., 1995). For a constant Q, Blanch et al. (1995) solve for estimating parameters. But for frequency-dependent Q, we must solve equation 4 numerically.

Viscoelastic wave equation

Here, we describe the basic velocity-stress formulation used later for the FD implementations. Derivation of these equations can be found, for instance, in Robertsson et al. (1994) and Carcione et al. (1988a, b). For a GZB model, the constitutive stress-strain relation in a Cartesian coordinate system $[x_1, x_2, x_3]$ is

$$\partial_t\sigma_{ij} = (\Pi - 2M)\partial_k v_k\delta_{ij} + M(\partial_i v_j + \partial_j v_i) + r_{ij}, \qquad (5)$$

where ∂_t and ∂_i denote partial derivatives with respect to time and spatial coordinate, respectively; $i,j,k = (1,2,3)$; δ_{ij} is the Kronecker delta; and v_i and σ_{ij} are particle velocity and stress components, respectively. Note in equation 5 that the summation convention has been applied. The unrelaxed moduli Π and M and memory variables r_{ij} are

$$\Pi = (\Lambda + 2M) = (\lambda_R + 2\mu_R)\left[1 - \frac{1}{L}\sum_{l=1}^{L}\left(1 - \frac{\tau_\varepsilon^{Pl}}{\tau_\sigma^l}\right)\right], \qquad (6)$$

$$M = \mu_R\left[1 - \frac{1}{L}\sum_{l=1}^{L}\left(1 - \frac{\tau_\varepsilon^{Sl}}{\tau_\sigma^l}\right)\right], \qquad (7)$$

$$r_{ij} = \frac{1}{L}\sum_{l=1}^{L} r_{ij}^l, \qquad (8)$$

where λ_R and μ_R are relaxed moduli, the superscripts P and S denote P- and S-waves. Equations for the memory variables are

$$\partial_t r_{ij}^l = -\frac{1}{\tau_\sigma^l}\Bigg\{ r_{ij}^l + \left[(\lambda_R + 2\mu_R)\left(\frac{\tau_\varepsilon^{Pl}}{\tau_\sigma^l} - 1\right) - 2\mu_R\left(\frac{\tau_\varepsilon^{Sl}}{\tau_\sigma^l} - 1\right)\right]\partial_k v_k \delta_{ij} + \left[\mu_R\left(\frac{\tau_\varepsilon^{Sl}}{\tau_\sigma^l} - 1\right)\right] \times (\partial_i v_j + \partial_j v_i)\Bigg\}. \quad (9)$$

For determining relaxed and unrelaxed moduli M_R and M_U, we use P- and S-wave phase velocities V_{P0} and V_{S0} at a reference angular frequency ω_0 as

$$\pi_R = (\lambda_R + 2\mu_R) = V_{P0}^2\,\rho\Re\left[\frac{L}{\sum_{l=1}^{L}\left(\frac{1 + i\omega_0\tau_\varepsilon^{Pl}}{1 + i\omega_0\tau_\sigma^l}\right)}\right], \quad (10)$$

$$\mu_R = V_{S0}^2\,\rho\Re\left[\frac{L}{\sum_{l=1}^{L}\left(\frac{1 + i\omega_0\tau_\varepsilon^{Sl}}{1 + i\omega_0\tau_\sigma^l}\right)}\right], \quad (11)$$

where ρ is density (e.g., Bohlen, 2002).

VISCOELASTODYNAMIC EQUATIONS FOR PLANE WAVES

Hereafter, we consider a Cartesian coordinate system in two dimensions (x_1,x_3) with downward positive x_3-direction. The general 2D velocity-stress viscoelastic wave equation may then be written as

$$\begin{aligned}
\rho\partial_t v_1 &= \partial_1\sigma_{11} + \partial_3\sigma_{13},\\
\rho\partial_t v_3 &= \partial_1\sigma_{31} + \partial_3\sigma_{33},\\
\partial_t\sigma_{11} &= (\Lambda + 2M)\partial_1 v_1 + \Lambda\partial_3 v_3 + r_{11},\\
\partial_t\sigma_{33} &= \Lambda\partial_1 v_1 + (\Lambda + 2M)\partial_3 v_3 + r_{33},\\
\partial_t\sigma_{13} &= M(\partial_3 v_1 + \partial_1 v_3) + r_{13},\\
\partial_t r_{11}^l &= -\frac{1}{\tau_\sigma^l}[r_{11}^l + (\Delta\pi^l - 2\Delta\mu^l)(\partial_1 v_1 + \partial_3 v_3) + 2\Delta\mu^l\partial_1 v_1],\\
\partial_t r_{33}^l &= -\frac{1}{\tau_{\sigma l}}[r_{33}^l + (\Delta\pi^l - 2\Delta\mu^l)(\partial_1 v_1 + \partial_3 v_3) + 2\Delta\mu^l\partial_3 v_3],\\
\partial_t r_{13}^l &= -\frac{1}{\tau_\sigma^l}[r_{13}^l + \Delta\mu^l(\partial_3 v_1 + \partial_1 v_3)],
\end{aligned} \quad (12)$$

where $\Delta\pi^l$ and $\Delta\mu^l$ are the difference between relaxed and unrelaxed moduli for each single relaxation:

$$\Delta\pi^l = \Pi - (\lambda_R + 2\mu_R) = (\lambda_R + 2\mu_R)\left(\frac{\tau_\varepsilon^{Pl}}{\tau_\sigma^l} - 1\right),$$

$$\Delta\mu^l = M - \mu_R = \mu_R\left(\frac{\tau_\varepsilon^{Sl}}{\tau_\sigma^l} - 1\right).$$

We now consider an incident plane-wave problem for a 1D heterogeneous medium where material properties are vertically heterogeneous but laterally invariant. With this simplification, we can replace the particle velocity and stress components with their slant-stack pairs using the inverse Radon transform (Chapman, 1981; McCowan and Brysk, 1989):

$$f(\tau,p) = \int f(\tau + px_1, x_1)dx_1, \quad (13)$$

where p is horizontal slowness, $\tau = t - px_1$, and $f(.)$ is a 2D function that, in this paper, is particle velocity or stress.

Substituting equation 13 into equation 12, followed by some manipulation using equations 6–9, we derive the velocity, stress, and memory-variable components for the viscoelastic medium in the plane-wave domain. A similar plane-wave approach was done by Blanch et al. (1998) for viscoacoustic media. They apply the Radon transform to the acoustic wave equation and derive a family of 1D wave equations that governs the evolution of wavefields in the plane-wave domain. We use the same technique to derive the plane-wave equations for the viscoelastic (P-SV) case for vertically heterogeneous attenuative media (see Appendix A for details).

FDTD COMPUTATIONS

To solve the plane-wave equations A-1 numerically, we exploit an FDTD technique with staggered grids in time and space.

FD scheme

For numerical solution of the wave equation, several staggered-grid FD schemes have been proposed for 2D and 3D elastic (Virieux, 1984, 1986; Levander, 1988; Graves, 1996) and viscoelastic media (Robertsson et al., 1994; Hestholm, 2002). Here, a 1D staggered-grid FD scheme with second-order accuracy in time and fourth-order accuracy in space, $O(\Delta t^2, \Delta x^4)$, is used, where Δt and Δx are temporal and spatial grid spacing, respectively.

Figure 1 illustrates the position of the wavefield variables in the 1D staggered-grid layout. By putting different velocity components on the free surface, two types of mesh grids may be used (type 1 and type 2) for the cases when the free-surface condition must be considered (Figure 1). In grid type 1, the horizontal component of particle velocity is on the free surface; in grid type 2, the vertical component is on the free surface.

Wavefield variables for the P-SV case are v_1, v_3, σ_{33}, σ_{13}, r_{11}, r_{33}, and r_{13}. The FD equations for P-SV plane waves are then

$$v_{3(i+1/2)}^{n+1/2} = v_{3(i+1/2)}^{n-1/2} - \Delta t\left(\frac{Mp}{\Delta_S}\right)D_{x_3}v_{1(i)}^n + \frac{\Delta t}{\Delta_S}D_{x_3}\sigma_{33(i)}^n - \frac{\Delta tp}{\Delta_S}\left(\frac{r_{13(i+1/2)}^{n+1/2} + r_{13(i+1/2)}^{n-1/2}}{2}\right), \quad (14)$$

$$r^{n+1/2l}_{13(i+1/2)} = \frac{2\tau^l_\sigma - \Delta t}{2\tau^l_\sigma + \Delta t} r^{n-1/2l}_{13(i+1/2)} - \frac{2\Delta\mu^l}{2\tau^l_\sigma + \Delta t} \times [- p(v^{n+1/2}_{3(i+1/2)} - v^{n-1/2}_{3(i+1/2)}) + \Delta t D_{x_3} v^n_{1(i)}], \tag{15}$$

$$\sigma^{n+1/2}_{13(i+1/2)} = \sigma^{n-1/2}_{13(i+1/2)} + \Delta t M\left(1 + \frac{Mp^2}{\Delta_S}\right) D_{x_3} v^n_{1(i)} - \Delta t\left(\frac{Mp}{\Delta_S}\right) D_{x_3}\sigma^n_{33(i)} + \Delta t\left(1 + \frac{Mp^2}{\Delta_S}\right) \times \left(\frac{r^{n+1/2}_{13(i+1/2)} + r^{n-1/2}_{13(i+1/2)}}{2}\right), \tag{16}$$

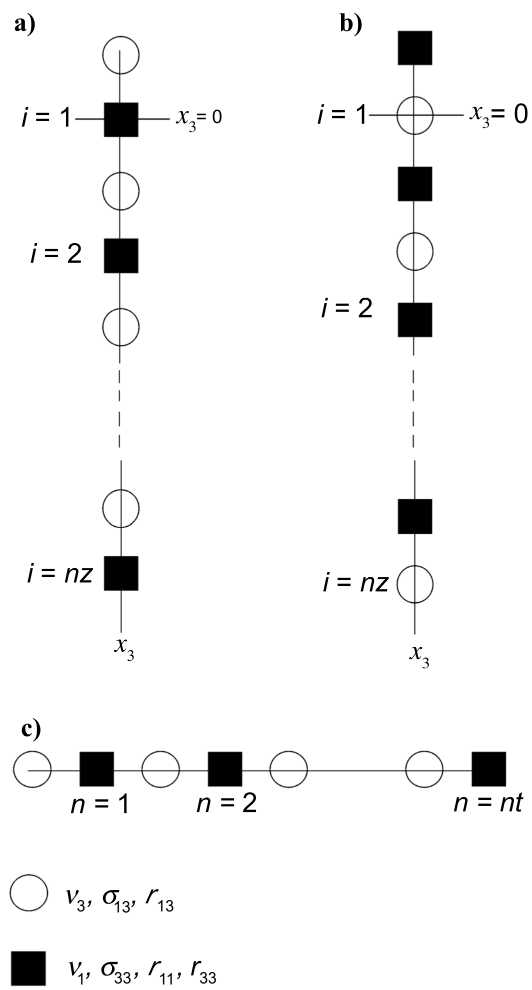

Figure 1. Arrangement of quantities for the staggered-grid scheme: (a) type 1, spatial arrangement; (b) type 2, spatial arrangement; and (c) temporal arrangement.

$$v^{n+1}_{1(i)} = v^n_{1(i)} - \Delta t\left(\frac{\Lambda p}{\Delta_P}\right) D_{x_3} v^{n+1/2}_{3(i+1/2)} + \frac{\Delta t}{\Delta_S}\left[1 + \frac{(\Lambda + M)p^2}{\Delta_P}\right] D_{x_3}\sigma^{n+1/2}_{13(i+1/2)} - \frac{\Delta t p}{\Delta_S}\left[1 + \frac{(\Lambda + M)p^2}{\Delta_P}\right]\left(\frac{r^{n+1}_{11(i)} + r^n_{11(i)}}{2}\right), \tag{17}$$

$$r^{n+1l}_{11(i)} = \frac{2\tau^l_\sigma - \Delta t}{2\tau^l_\sigma + \Delta t} r^{nl}_{11(i)} - \frac{2\Delta\pi^l}{2\tau^l_\sigma + \Delta t}[- p(v^{n+1}_{1(i)} - v^n_{1(i)}) + \Delta t D_{x_3} v^{n+1/2}_{3(i+1/2)}] + \frac{4\Delta\mu^l}{2\tau^l_\sigma + \Delta t}\Delta t D_{x_3} v^{n+1/2}_{3(i+1/2)}, \tag{18}$$

$$r^{n+1l}_{33(i)} = \frac{2\tau^l_\sigma - \Delta t}{2\tau^l_\sigma + \Delta t} r^{nl}_{33(i)} - \frac{2\Delta\pi^l}{2\tau^l_\sigma + \Delta t}[- p(v^{n+1}_{1(i)} - v^n_{1(i)}) + \Delta t D_{x_3} v^{n+1/2}_{3(i+1/2)}] - \frac{4p\Delta\mu^l}{2\tau^l_\sigma + \Delta t}(v^{n+1}_{1(i)} - v^n_{1(i)}), \tag{19}$$

$$\sigma^{n+1}_{33(i)} = \sigma^n_{33(i)} + \Delta t\left(\Pi + \frac{\Lambda^2 p^2}{\Delta_P}\right) D_{x_3} v^{n+1/2}_{3(i+1/2)} - \Delta t\left(\frac{\Lambda p}{\Delta_P}\right) D_{x_3}\sigma^{n+1/2}_{13(i+1/2)} + \Delta t\left(\frac{r^{n+1}_{33(i)} + r^n_{33(i)}}{2}\right) + \Delta t\left(\frac{\Lambda p^2}{\Delta_P}\right)\left(\frac{r^{n+1}_{11(i)} + r^n_{11(i)}}{2}\right), \tag{20}$$

where D_{x_3} is the finite-difference operator in the x_3-direction (Appendix B). In equations 14–20, n and (i) are time and spatial indices, respectively. Using grid type 1, which is used for calculating numerical examples in the later section, the depth x_3 and time t for v_1, σ_{33}, r_{11}, and r_{33} are $x_3 = (i - 1)\Delta x$ and $t = n\Delta t$, respectively. For v_3, σ_{13}, and r_{13}, the depth is $x_3 = (i - 1/2)\Delta x$ and $t = (n - 1/2)\Delta t$. For grid type 2, vertical and horizontal components of particle velocity will exchange their position both in time and space.

Equations 14–20 are implicit with respect to $v_{1(i)}$ and $r_{11(i)}$ and also $v_{3(i+1/2)}$ and $r_{13(i+1/2)}$. There are two ways to construct a fully explicit scheme. We can approximate the future values on the right-hand side with available past values (we call this strategy method A), or we can rearrange the equations to eliminate the future values on the right-hand side (method B). The first way replaces $r^{n+1/2}_{13(i+1/2)}$ by $r^{n-1/2}_{13(i+1/2)}$ in equation 14 and $r^{n+1}_{11(i)}$ by $r^n_{11(i)}$ in equation 17, so that equations 14–20 become fully explicit. Method B is described in Appendix C.

It is worth mentioning that the calculated waveforms by the schemes are in the propagating regime as long as Δ_P and Δ_S are positive. In other words, when $p < \sqrt{\rho/\Pi}$ and $p < \sqrt{\rho/M}$, then the values of Δ_P and Δ_S are positive and the P and S plane waves are both propagating (nonevanescent). If $p > \sqrt{\rho/\Pi}$ and/or $p > \sqrt{\rho/M}$, then the values of Δ_P and/or Δ_S are negative and the P and/or S plane waves are evanescent, in which case our proposed 1D FDTD method is unable to represent them. Figure 2 shows the variation of Δ_P and Δ_S with horizontal slowness for a homogeneous half-space of $\rho = 2$ g/cm^3, $\Pi = 17.34$ GPa, and $M = 4.63$ GPa.

Boundary conditions

In the grid layout shown in Figure 1, the boundaries to be considered are a free-surface and/or radiation boundary (nonreflecting boundary) at the top and/or bottom of the model. The grid is one dimensional, so it is unnecessary to deal with the side boundaries of the structure model, and there are no artificial side reflections. The free surface is implemented by applying the so-called image methods (Levander, 1988; Robertsson, 1996), which extend the grid half a sample above the free surface. Robertsson (1996) summarizes the possibilities for treating particle velocity and stress components above the free surface, which are formally required by the FD scheme as image methods 1, 2, and 3. Tanaka and Takenaka (2005) show that using particle velocity as an even function and stress as an odd function with respect to the free surface (image method 2) gives a better result than setting only the stress components as an odd function with respect to the free surface and the particle velocity to zero above the free surface (image method 3).

In the present paper, we use image method 2. Components of particle velocity, stress, and memory variables on the free surface are different between the two grid types shown in Figure 1. In type 1, v_1, σ_{33}, r_{11}, and r_{33} are on the free surface, whereas in type 2, v_3, σ_{13}, and r_{13} are located there.

To implement a nonreflecting boundary, we apply the absorbing-zone technique of Cerjan et al. (1985) and the first-order, one-way wave equation techniques of Clayton and Engquist (1977). In the proposed algorithm, the nonreflecting boundary is implemented at the bottom and/or at the top of the model. The nonreflecting boundary at the bottom of the model is fixed, but the boundary at the top can be chosen to be either a free surface or a nonreflecting boundary.

Stability and numerical dispersion

For a stable FD scheme, the temporal grid size is chosen in accordance with the rule outlined by Levander (1988) as $\Delta t < 0.606\Delta x_i/c$ (where c is the velocity) for the $O(\Delta t^2, \Delta x^4)$ scheme. However, for choosing the proper value of grid spacing for the viscoelastic scheme, the Courant number ($c\Delta t/\Delta x_i$) must be adjusted to the highest phase velocity (Robertsson et al., 1994), which for our P-SV case is $c_{\max} = 1/\min(\eta_\alpha)$, where η_α is the vertical slowness of the P-wave that is calculated by $\eta_\alpha = \sqrt{(\rho/\Pi) - p^2}$. To minimize the effect of grid dispersion, the fourth-order system also requires a minimum sampling of five grid points/wavelength (Levander, 1988).

Initial wave zone

The grid of the proposed algorithm is divided into two parts: an initial wave zone and a computational domain. For the incident wave, we consider an attenuation-free (perfect elastic) homogeneous zone. This zone can be set on top of or under the computational domain. The initial wave zone should have no velocity contrast with its adjacent layer of the computational domain to prevent artificial reflections and conversions. However, the Q contrast may cause a negligibly weak reflection in the case of very-high-attenuation models. The thickness of the initial wave zone should be larger than the total width of the incident plane wave and the absorbing zone. The absorbing zone occupies 50 grid points in the examples shown in the next section.

NUMERICAL EXAMPLES

In this section, we examine the performance of the proposed algorithm by running five numerical examples. The first example demonstrates the accuracy of our FD schemes by comparing results from FD computations and an analytical solution in the time domain. For the analytical solution of the plane wave, we use the solution obtained by Blanch et al. (1995). They incorporate constant Q as a function of frequency analytically via Futterman's (1962) expression. In the solution of Blanch et al. (1995), the incident angle is not considered; so in the case of oblique incidence in a homogeneous medium, we use apparent velocity as propagation speed.

The second example successfully incorporates attenuation into the computational algorithm even for a very highly attenuative medium. The third example demonstrates results for grid types 1 and 2 on the free surface and the analytical solution. For the analytical solution on the free surface, we use the free-surface amplification factors (e.g., Kennett, 2001).

In the fourth example, to illustrate the efficiency of the algorithm as compared to 2D FD computations, we calculate a VSP using a conventional 2D FDTD and our proposed 1D FD scheme. In the final example, the ability of the algorithm for calculating plane-wave responses of a vertically heterogeneous attenuative medium is demonstrated by calculating a synthetic VSP for a borehole in the Kanto area of Japan.

Accuracy test

To check the accuracy of our FD calculations, the result from a numerical simulation is compared with the corresponding analytical solution. The structure model is a homogeneous attenuative medium. The P-wave velocity is 2000 m/s at the reference frequency of $f_0 = 20$ Hz and density of 2.0 g/cm^3. The attenuation model is a constant $Q = 50$, which is modeled by five Zener bodies. In this example, the top and bottom boundaries of the model are set to be nonreflecting. A Ricker wavelet with a central frequency of 20 Hz and

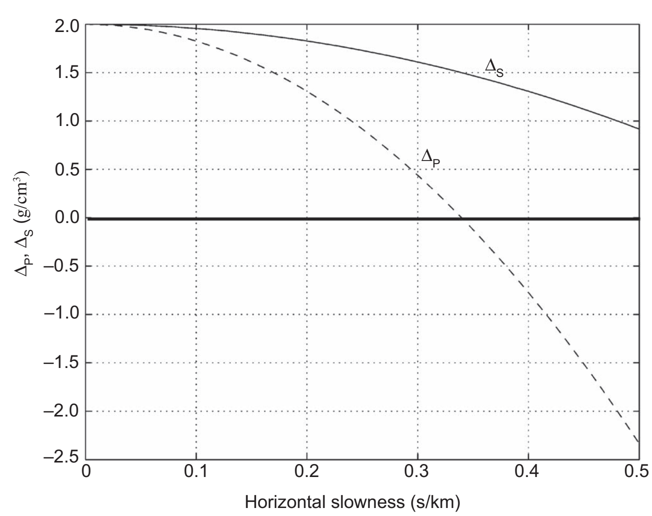

Figure 2. Variation of Δ_P and Δ_S with respect to the horizontal slowness in a homogeneous half-space ($\rho = 2$ g/cm^3, $\Pi = 17.34$ GPa, and $M = 4.63$ GPa).

an incident angle θ of 20° is set at a depth of 1 km in the initial wave zone as the incident P-wave, and the receiver is placed at a depth of 2.0 km. The computational domain starts from a depth of 1.05 km. The exact location of the vertical component is half a grid step below the horizontal component, so the distance of propagation for horizontal and vertical components is 0.950 and 0.9525 km, respectively. The time increment and spatial grid interval are $\Delta t = 1$ ms and $\Delta x = 5$ m, respectively. The total number of time steps and grid points is 2000 and 600, respectively.

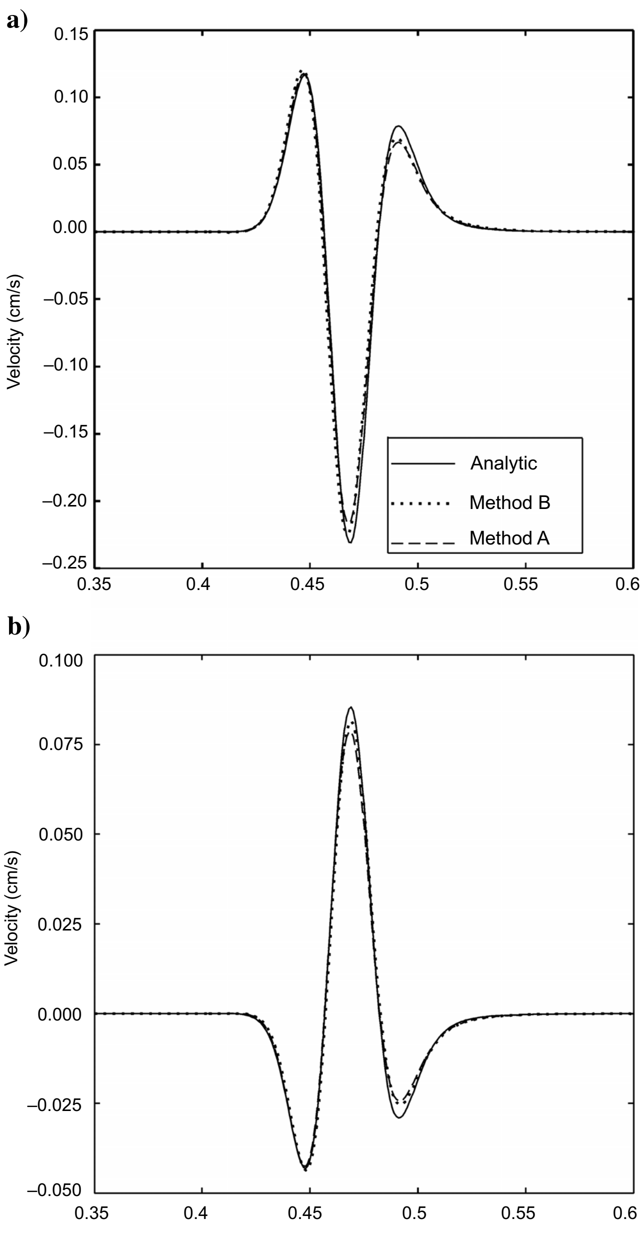

Figure 3. Synthetic waveforms calculated by the two proposed FD methods and the analytical solution for a half-space with properties explained in the text. The calculated waveforms by methods A and B are shown by dashed and dotted lines, respectively. The analytical solution is shown by the solid line. (a) Vertical component. (b) Horizontal component.

We run the computations for two proposed FD schemes (methods A and B). Calculated waveforms from the two methods are compared with the analytical solution in Figure 3. The two methods simulate the analytical solution almost equally well. The discrepancy of the FD solutions from the analytical solutions may be mainly because of the difference of the attenuation models between the FDM methods and the analytical solution. The FD methods are based on the GZB, but the analytical solution is based on Futtermann's operator.

Because the two methods show a similar degree of accuracy resulting from its simplicity, we hereafter use method A for computations. Although method A is an approximation, it is very accurate for any time increment Δt satisfying the stability condition. We have not experienced its breakdown yet. The related code to this article is based on method A. One can run the attached code with the default values of parameters given in the code and derive vertical and horizontal components of synthetic particle velocity shown in Figure 3. Instructions for running the code are given in the README file included with the code.

Attenuation incorporation test

The accuracy of attenuation incorporation and dispersion modeling is investigated by comparing the target Q and velocity dispersion curve modeled by five Zener bodies with the measured apparent Q and velocity. For this example, two cases are considered: a very attenuative model with $Q \approx 7$ and a moderately attenuative model with $Q \approx 55$ (Figure 4). The frequency-dependent apparent Q factor and velocity are measured from the calculated seismograms at two successive positions of 1.5 and 2.5 km depth in a homogeneous medium. Material properties of the medium are the same as those of the first numerical example. The FD scheme and the incident plane wave are also the same as in the first numerical example.

Figure 4 shows the comparison of measured and target Q and apparent velocities (calculated for GZB) for very attenuative ($Q \approx 7$) and moderately attenuative ($Q \approx 55$) media. The differences between the measured and target Q are less than 8% in the frequency

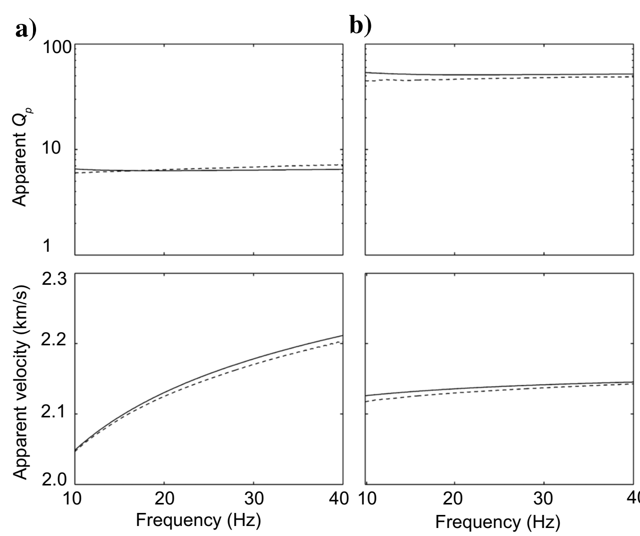

Figure 4. Comparison between the observed (dashed lines) and the target (solid lines) frequency-dependent apparent Q and the apparent velocity for (a) highly attenuative and (b) moderately attenuative media.

range of interest, 10–40 Hz for both models. The estimated apparent velocities match the target ones (calculated using GZBs) very well, with less than 1% differences. These results demonstrate that the proposed algorithm is fairly accurate even for very attenuative media.

Grid types

To examine the performance of the two different FD grids shown in Figure 1 (types 1 and 2) we compute the free-surface response of a homogeneous half-space using the two FD grid systems shown in Figure 1. The P- and S-wave velocities of the half-space are 2650 and 1500 m/s at $f_0 = 20$ (Hz), respectively, and density is 2.0 g/cm^3. The incident wave is an inclined upgoing P-wave ($\theta = 20°$). In this example, the bottom boundary of the model is nonreflecting and the top is a free surface. The initial wave is a phaseless Ricker wavelet with a central frequency of 20 Hz, set at a depth of 2.0 km. The initial wave zone ($x_3 > 1.935$ km) is under the computational domain.

Figure 5 shows the comparison between the FD and analytical solutions. Recall that in grid type 1, the vertical velocity is located not on the free surface but at half a grid step below the free surface, and in type 2 the horizontal velocity is located not on the free surface but at half a grid step below the free surface. In Figure 5 the vertical component of surface velocity from type 1 is almost identical to the corresponding waveform from type 2, although the corresponding horizontal components from the two grid systems have a slight difference. This result suggests that type 1 is preferable to type 2 if only one grid system is used for simulations.

Efficiency test

We show the efficiency of the algorithm by comparing the plane-wave response of a simple one-layer model to an upgoing oblique incident P-wave ($\theta = 20°$) calculated by the proposed 1D FD scheme and a conventional 2D FD scheme. The 2D viscoelastic FDTD is second-order accurate in time and fourth-order accurate in space $O(\Delta t^2, \Delta x^4)$. A memory-variable technique (Robertsson et al., 1994; Blanch et al., 1995) is applied for incorporating attenuation into the scheme. To implement the nonreflecting boundary condition on the side and bottom boundaries of 2D FD computation, the absorbing-zone technique of Cerjan et al. (1985) and the first-order, one-way wave-equation techniques of Clayton and Engquist (1977) are applied. The top boundary is the free surface. In the 1D computation, the bottom boundary is nonreflecting and the top boundary is free surface.

The initial wave is a Ricker wavelet with a central frequency of 50 Hz. The model consists of a 100-m-thick attenuative layer of $Q_P = 50$ and $Q_S = 25$ (incorporated into the FD schemes by one Zener body) overlying an elastic half-space. P-wave velocities and densities at the reference frequency of 20 Hz are $V_{P0} = 1.7$ km/s, $\rho = 2.3$ g/cm^3 for the layer and $V_{P0} = 2.5$ km/s, $\rho = 2.4$ g/cm^3 for the underlaying half-space. The S-wave velocities are set to be $V_{S0} = V_{P0}/\sqrt{3}$.

Figure 6 shows the vertical components of a calculated VSP for the model using the conventional 2D FDTD and the proposed 1D FDTD. In the case of 2D computation, the medium was discretized into a 400×400 grid with vertical and horizontal grid intervals of 1 m. For the 1D computation, only 400 grid points with $\Delta x = 1$ m were used. The time increment was set to $\Delta t = 0.2$ ms for both 1D and 2D calculations. Clearly, the computational costs drastically increase using 2D FDTD instead of 1D FDTD for layered 1D media. Although in the 2D case we have picked the calculated waveforms at the middle of the mesh to avoid the artificial side reflections, several artificial reflection phases from the side boundaries are still seen on the 2D FD computation results (Figure 6a). One-dimensional FD waveforms produce a very-high-quality profile (Figure 6b).

A synthetic VSP

To demonstrate the performance of the proposed algorithm, we generate a plane-wave synthetic VSP for a vertically heterogeneous attenuative medium. The model is a 2781-m-deep sedimentary sys-

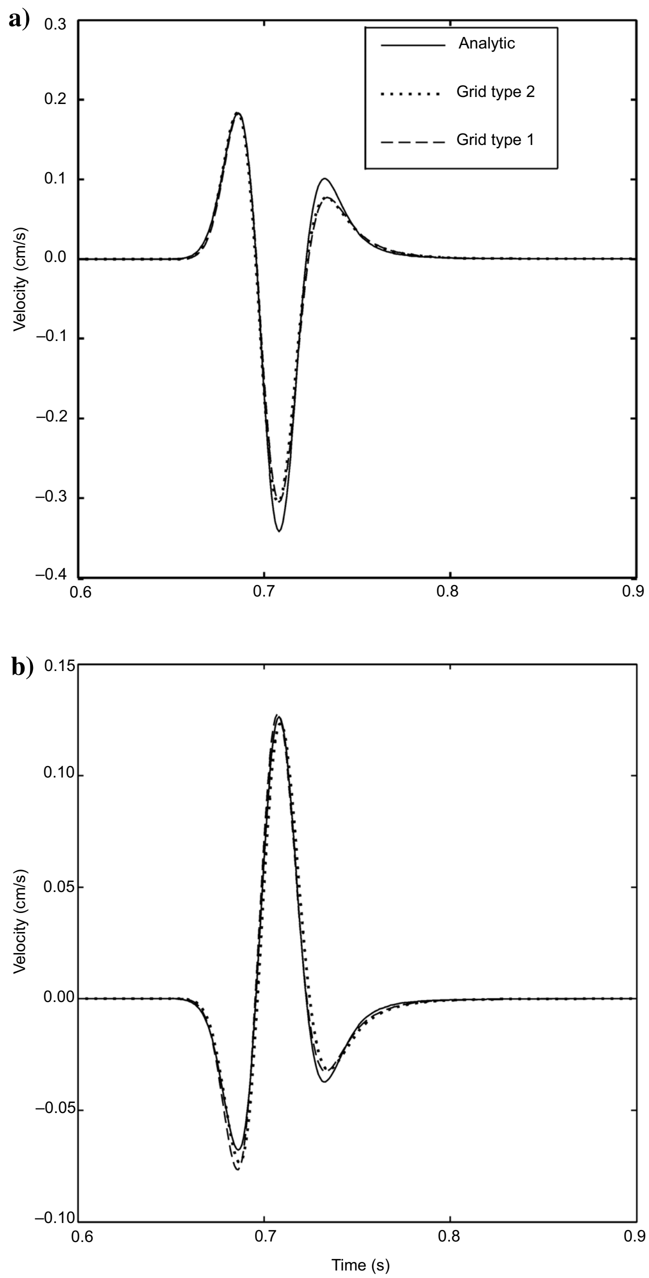

Figure 5. Vertical and horizontal components of synthetic waveforms calculated by two different FD grid types and the analytical solution. The calculated waveforms by analytical solution, type 1, and type 2 are shown by solid, dashed, and dotted lines, respectively. (a) Vertical component. (b) Horizontal component.

tem (including sediments and basement) in the Kanto area, Japan. The velocity structure (Figure 7) is created from well-log data from the Fuchu borehole (Suzuki et al., 1981) and the velocity model estimated by Yamamizu et al. (1981). Since the well-log data are available only for the interval between 500 and 2780 m, this interval is considered as the computational target domain, and the synthetic seismograms are generated for this interval. Attenuation behavior of the system has been studied by Kinoshita and Ohike (2002). They estimate a frequency-dependent Q_S as in the frequency range of 0.5–16 Hz. Stork and Ito (2004) show that the ratio of Q_P^{-1}/Q_S^{-1} is about 1.5 for the frequency range between 10 and 60 Hz in western Nagano, a neighboring prefecture of the Kanto area. For our simulation, we use a frequency-dependent Q_P^{-1} shown in Figure 8 and $Q_P^{-1}/Q_S^{-1} \approx 1.5$. To model Q_P^{-1} as well as Q_S^{-1}, we employ five relaxation mechanisms in the form of GZB.

For FD simulation, $\Delta x = 5$ m and $\Delta t = 0.1$ ms are used. The original velocity and density data were digitized with a sampling interval of 1 m (Suzuki et al., 1981), so an averaging technique proposed by Moczo et al. (2002) is used to incorporate the subgrid structure of velocities and density into the FD grid. This technique helps to achieve accurate arrival times. A Ricker wavelet with a central frequency of 20 Hz is used as an incident P-wave. P- and S-wave velocities of the model correspond to those at the reference frequency of $f_0 = 20$ Hz. The initial wave zone is overlain on the computational domain. To reduce artificial reflections and conversions at the interface between the initial wave zone and the computational target domain, we use the average velocities and density of the top 50 m of the computational target domain as the velocities and density of the initial wave zone. The nonreflecting boundary condition is used for both the top and bottom of the model. The simulation is done for elastic and viscoelastic cases both for normal and inclined incident plane waves. Receivers are located at 46 levels in 50-m intervals from 500 to 2800 m deep in the borehole. In the case of oblique incidence, an incident angle of 20° is used.

Figure 9a and b shows the vertical components of synthetic VSP to the normal incident wave for elastic and viscoelastic cases, respectively. In this figure, two main reflections can be seen: one from a depth of about 1000 m and the other from about 2000 m. However, in the viscoelastic case (Figure 9b) because of the strong attenuation, the amplitudes of reflected waves are much decreased. According to the geological log at Fuchu borehole (Suzuki et al., 1981; Yamamizu et al., 1981), the lithology below 2000 m is sandstone, slate, and quartzite, which comprise the pre-Tertiary basement of the sedimen-

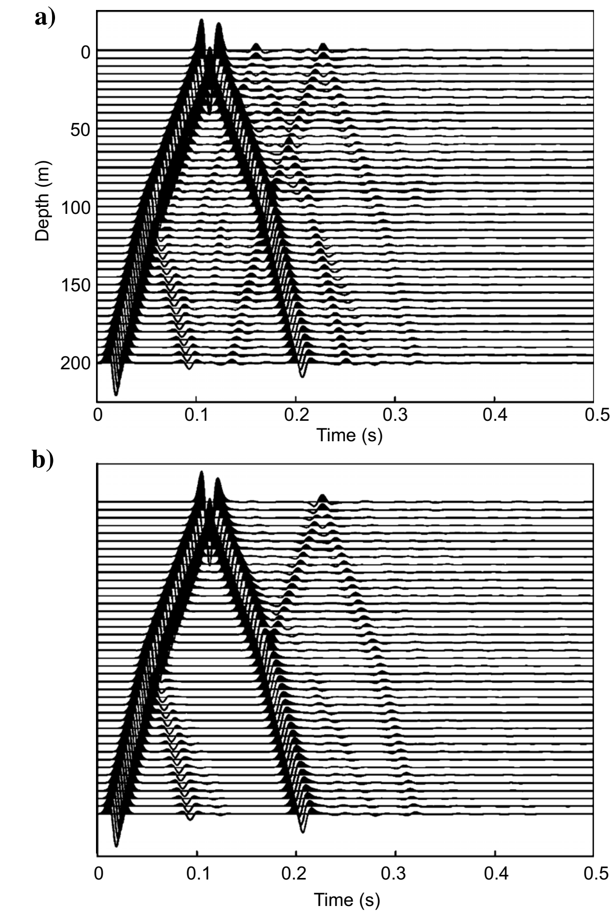

Figure 6. Comparison of the plane-wave responses (vertical component) of a one-layer structure calculated by (a) a conventional 2D FDTD scheme and (b) our proposed 1D FDTD algorithm.

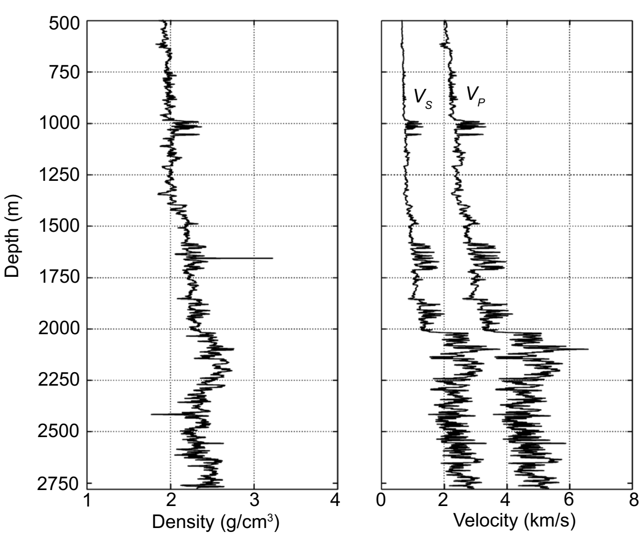

Figure 7. Velocity and density structural model of the Fuchu borehole site, Japan, made from well-log (Suzuki et al., 1981) and borehole seismic exploration data (Yamamizu et al., 1981).

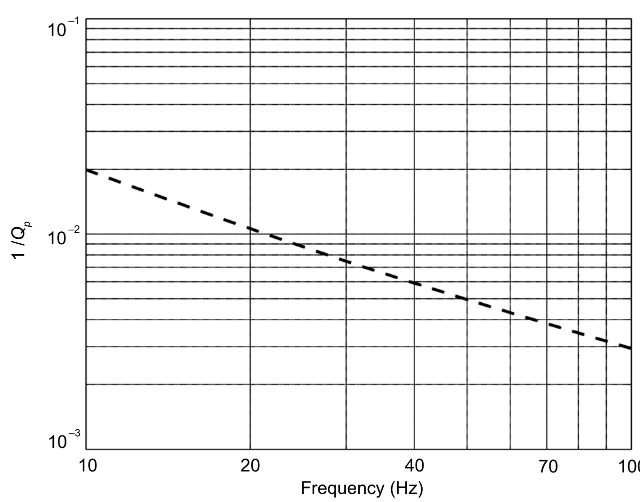

Figure 8. Frequency-dependent Q model for the sedimentary system at the Fuchu borehole site used for the FD simulations.

tary system. Lying on the basement up to 1000 m is the Miocene Miura Group. This group includes sedimentary layers and sublayers of sand, silt, mud, granule sandstone, and tuff. The contrast between the basement and the Miura Group creates a stronger reflection than the contrast at the boundary at about 1000 m.

Figure 9c and d shows the simulation results for the inclined-incidence example for elastic and viscoelastic cases, respectively. In the cases of inclined incidence, the conversions happen at the boundaries. But according to the smaller amplitude of converted waves and lack of strong contrast in the model, it is difficult to distinguish them on the vertical components except for the structural discontinuity at a depth of 2000 m, where the downgoing converted S-wave is visible. However, it is easy to distinguish the converted S-wave on the horizontal components. Figure 10 shows the horizontal components of the simulation; the upgoing and downgoing converted S waves can be seen clearly for the main contrasts of the model.

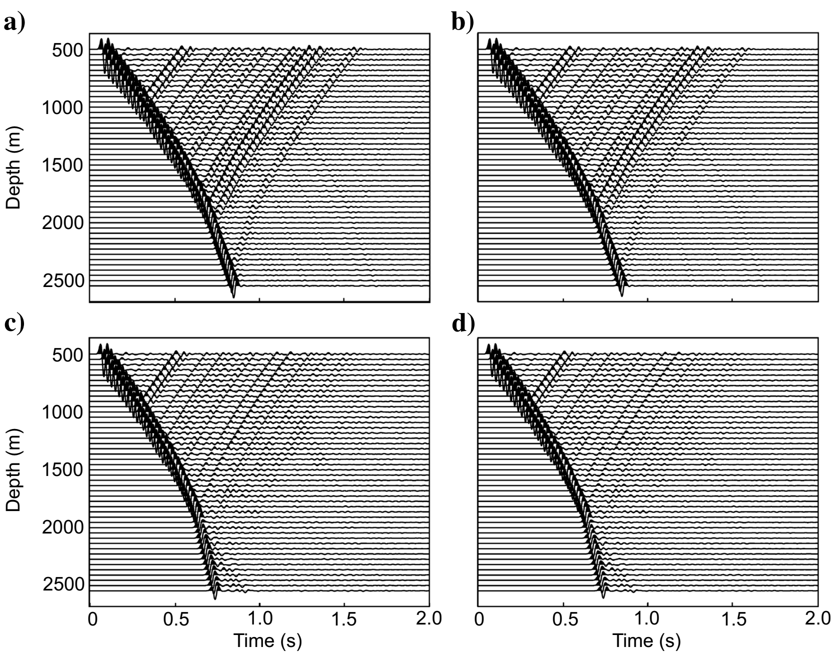

Figure 9. Vertical components of synthetic plane-wave VSP for the Fuchu borehole site. (a) Elastic and (b) viscoelastic responses of the model to a normal incident P-wave; (c) elastic and (d) viscoelastic responses of the model to an inclined incident P-wave ($\theta = 20°$).

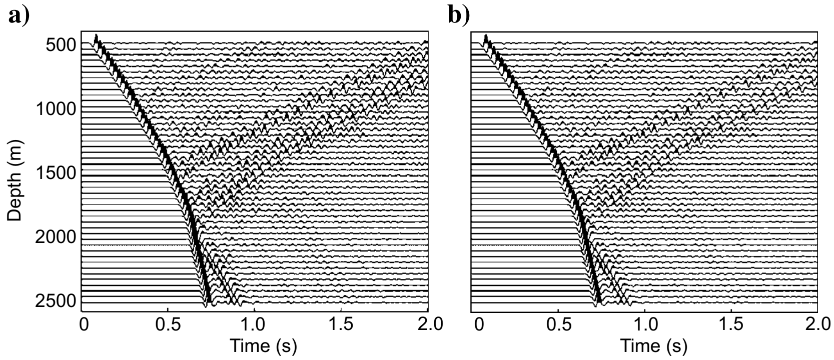

Figure 10. Horizontal components of synthetic plane-wave VSP for the Fuchu borehole site for (a) elastic and (b) viscoelastic responses to an inclined incident P-wave ($\theta = 20°$).

CONCLUSION

We have developed an efficient algorithm to calculate the plane-wave response of a vertically heterogeneous attenuative medium. The plane-wave equations are derived by applying the Radon transform to the 2D viscoelastic wave equation for 1D structures. The FDTD staggered-grid scheme is exploited to solve the plane-wave equations numerically. Our derived FD equations are implicit with respect to the particle velocity and memory variable components. We also derive two forms of fully explicit FD equations using two different approaches, which we call method A and method B. Comparison of simulation results from the two methods shows that their differences are negligible, and both methods can be used for simulation with enough accuracy. However, for simplicity, the attached code of our proposed algorithm is based on method A. In the proposed algorithm, the domain boundaries are only at the top and bottom. The lack of artificial side reflections is another advantage of this approach.

The accuracy of viscoelastic simulation by the proposed algorithm has been tested by comparing observed frequency-dependent Q and apparent velocity to the target ones. The results show very good agreement over a reasonably wide frequency range, even for very attenuative media. The proposed algorithm can be used to estimate the plane-wave responses of models with vertical velocity fluctuations such as borehole well-log data. Using the proposed algorithm to calculate a synthetic VSP for a borehole in the Kanto area of Japan shows that the algorithm can efficiently simulate reflected, transmitted, and converted waves for a heterogeneous medium with strong velocity contrasts.

Our proposed algorithm for synthesizing plane-wave seismograms in viscoelastic media may be used efficiently as a basis for linear inversion algorithms of short-scale elastic parameter fluctuations. This linear inversion may be regarded as a model-based analog of AVO processing and will be the subject of future research.

ACKNOWLEDGMENTS

I wish to thank editor J. Carcione, associate editor J. Dellinger, and four anonymous reviewers for valuable comments. J. Dellinger kindly helped us to improve the English statements in the README of the code. This study was supported partially by JSPS.KAKENHI (16540389) and the Earthquake Research Institute of the University of Tokyo, cooperative research program (2005-G-24).

APPENDIX A

VISCOELASTIC WAVE EQUATION IN THE PLANE-WAVE DOMAIN

The plane-wave equation can be derived by applying the Radon transform to equation 12. Using the Radon transform, the spatial differential operator with respect to x_1, ∂_1, is replaced by a temporal differential operator $-p\partial_t$. Moving all time derivatives to the left-hand side and all spatial derivatives ∂_{x_3} to the right-hand side of the equations, we derive the following equations in the plane-wave domain after further manipulation:

$$\begin{aligned}
\partial_t v_1 &= -\left(\frac{\Lambda p}{\Delta_P}\right)\partial_3 v_3 + \frac{1}{\Delta_S}\left[1 + \frac{(\Lambda + M)p^2}{\Delta_P}\right]\partial_3\sigma_{13} \\
&\quad - \frac{p}{\Delta_S}\left[1 + \frac{(\Lambda + M)p^2}{\Delta_P}\right]r_{11}, \\
\partial_t v_3 &= -\left(\frac{Mp}{\Delta_S}\right)\partial_3 v_1 + \left(\frac{1}{\Delta_S}\right)\partial_3\sigma_{33} - \left(\frac{p}{\Delta_S}\right)r_{13}, \\
\partial_t\sigma_{33} &= \left(\Pi + \frac{\Lambda^2 p^2}{\Delta_P}\right)\partial_3 v_3 - \left(\frac{\Lambda p}{\Delta_P}\right)\partial_3\sigma_{13} + r_{33} \\
&\quad + \left(\frac{\Lambda p^2}{\Delta_P}\right)r_{11}, \\
\partial_t\sigma_{13} &= M\left(1 + \frac{Mp^2}{\Delta_S}\right)\partial_3 v_1 - \left(\frac{Mp}{\Delta_S}\right)\partial_3\sigma_{33} \\
&\quad + \left(1 + \frac{Mp^2}{\Delta_S}\right)r_{13}, \\
\partial_t r_{11}^l &= -\frac{1}{\tau_\sigma^l}[r_{11}^l + (\Delta\pi^l - 2\Delta\mu^l)(-p\partial_t v_1 + \partial_3 v_3) \\
&\quad - 2p\Delta\mu^l\partial_t v_1], \\
\partial_t r_{33}^l &= -\frac{1}{\tau_\sigma^l}[r_{33}^l + (\Delta\pi^l - 2\Delta\mu^l)(-p\partial_t v_1 + \partial_3 v_3) \\
&\quad + 2\Delta\mu^l\partial_3 v_3], \\
\partial_t r_{13}^l &= -\frac{1}{\tau_\sigma^l}[r_{13}^l + \Delta\mu^l(-p\partial_t v_3 + \partial_3 v_1)],
\end{aligned} \tag{A-1}$$

where $\Delta_P = \rho - \Pi p^2$ and $\Delta_S = \rho - Mp^2$.

APPENDIX B

SPATIAL FINITE-DIFFERENCE OPERATORS

The fourth-order spatial FD operator of a function Ψ is

$$\begin{aligned}
D_{x_3}\Psi_{(i+1/2)} &= \frac{1}{\Delta x_3}\left[\frac{9}{8}(\Psi_{(i+1/2)} - \Psi_{(i-1/2)})\right. \\
&\quad \left. - \frac{1}{24}(\Psi_{(i+3/2)} - \Psi_{(i-3/2)})\right],
\end{aligned} \tag{B-1}$$

(Levander, 1988), and the second-order one is

$$D_{x_3}\Psi_{(i+1/2)} = \frac{1}{\Delta x_3}(\Psi_{(i+1)} - \Psi_{(i)}) \tag{B-2}$$

(Virieux, 1986).

APPENDIX C

ANOTHER FULLY EXPLICIT FD SCHEME (METHOD B)

Equations 14–20 are implicit with respect to $v_{1(i)}$ and $r_{11(i)}$ and also $v_{3(i+1/2)}$ and $r_{13(i+1/2)}$. Substituting equation 15 into equation 14 and rearranging the expression for $v_{3(i+1/2)}^{n+1/2}$, we obtain the equation for $v_{3(i+1/2)}^{n+1/2}$ (equation C-1). Substituting equation 18 into equation 17 and rearranging the expression for $v_{1(i)}^{n+1}$, we obtain the equation for $v_{1(i)}^{n+1}$ (equation C-2):

$$\begin{aligned}
v_{3(i+1/2)}^{n+1/2} &= v_{3(i+1/2)}^{n-1/2} + \frac{\Delta t}{1 + \dfrac{\Delta t p^2}{\Delta_S}A2_{(i+1/2)}} \\
&\quad \times\left[\left(\frac{\Delta t p}{\Delta_S}A2_{(i+1/2)} - \frac{Mp}{\Delta_P}\right)D_{x_3}v_{1(i)}^n\right. \\
&\quad \left. + \frac{1}{\Delta_S}D_{x_3}\sigma_{33(i)}^n - \frac{p}{\Delta_S}A3_{(i+1/2)}r_{13(i+1/2)}^{n-1/2}\right],
\end{aligned} \tag{C-1}$$

$$\begin{aligned}
v_{1(i)}^{n+1} &= v_{1(i)}^n + \frac{\Delta t}{1 + \dfrac{\Delta t p^2}{\Delta_S}\left[1 + \dfrac{(\Lambda + M)p^2}{\Delta_P}\right]A1_{(i)}} \\
&\quad \times\left\{\left\{\frac{\Delta t p}{\Delta_S}\left[1 + \frac{(\Lambda + M)p^2}{\Delta_P}\right](A1_{(i)} - 2A2_{(i)})\right.\right. \\
&\quad \left. - \left(\frac{\Lambda p}{\Delta_P}\right)\right\}D_{x_3}v_{3(i+1/2)}^{n+1/2} + \frac{1}{\Delta_S}\left[1 + \frac{(\Lambda + M)p^2}{\Delta_P}\right] \\
&\quad \left.\times D_{x_3}\sigma_{13(i+1/2)}^{n+1/2} - \frac{p}{\Delta_S}\left[1 + \frac{(\Lambda + M)p^2}{\Delta_P}\right]A3_{(i)}r_{11(i)}^n\right\},
\end{aligned} \tag{C-2}$$

where

$$\begin{aligned}
A1 &= \frac{1}{2L}\sum_{l=1}^{L}\frac{2\Delta\pi^l}{2\tau_\sigma^l + \Delta t}, \\
A2 &= \frac{1}{2L}\sum_{l=1}^{L}\frac{2\Delta\mu^l}{2\tau_\sigma^l + \Delta t}, \\
A3 &= \frac{1}{2L}\sum_{l=1}^{L}\left(\frac{2\tau_\sigma^l - \Delta t}{2\tau_\sigma^l + \Delta t} + 1\right).
\end{aligned} \tag{C-3}$$

Method B uses equations C-1, 15, 16, C-2, and 18–20.

REFERENCES

Aminzadeh, F., and J. M. Mendel, 1985, Synthetic vertical seismic profiles for nonnormal incident plane waves: Geophysics, **50**, 127–141.

Asvadorov, S., L. Knizhnerman, and J. Pabon, 2004, Finite-difference modeling of viscoelastic materials with quality factor of arbitrary magnitude: Geophysics, **69**, 817–824.

Blanch, J. O., J. O. A. Robertsson, and W. W. Symes, 1995, Modeling of a constant *Q*: Methodology and algorithm for an efficient and optimally inexpensive viscoelastic technique: Geophysics, **60**, 176–184.

Blanch, J. O., W. W. Symes, and R. J. Versteeg, 1998, A numerical study of linear viscoacoustic inversion, *in* R. G. Keys and D. J. Foster, eds., Comparison of seismic inversion methods on a single real data set: SEG, 13–44.

Blangy, J. P., 1994, AVO in transversely isotropic media—An overview: Geophysics, **49**, 775–781.

Bohlen, T., 2002, Parallel 3-D viscoelastic finite difference seismic modelling: Computer and Geosciences, **28**, 887–899.

Carcione, J. M., 2001, Wave fields in real media: Wave propagation in anisotropic, anelastic and porous media: Elsevier Science Publ. Co., Inc..

Carcione, J. M., D. Kosloff, and R. Kosloff, 1988a, Wave propagation simulation in a linear viscoelastic medium: Geophysical Journal of the Royal Astronomical Society, **93**, 393–407.

———, 1988b, Wave propagation simulation in a linear viscoelastic medium: Geophysical Journal of the Royal Astronomical Society, **95**, 597–611.

Cerjan, C., D. Kosloff, R. Kosloff, and M. Reshef, 1985, A nonreflecting boundary condition for discrete acoustic and elastic wave equations: Geophysics, **50**, 705–708.

Chapman, C. H., 1981, Generalized Radon transform and slant stacks: Geophysical Journal of the Royal Astronomical Society, **66**, 445–453.

Christensen, R. M., 1982, Theory of viscoelasticity: Dover Publ. Inc.

Clayton, R. W., and B. Engquist, 1977, Absorbing boundary conditions for acoustic and elastic wave equations: Bulletin of the Seismological Society of America, **67**, 1529–1540.

Dasgupta, R., and R. A. Clark, 1998, Estimation of *Q* from surface seismic reflection data: Geophysics, **63**, 2120–2128.

Day, S. M., and J. B. Minster, 1984, Numerical simulation of wavefields using a Padé approximant method: Geophysical Journal of the Royal Astronomical Society, **78**, 105–118.

Dietrich, M., 1990, An algorithm for the plane-wave decomposition of point-source seismograms: Geophysics, **55**, 1380–1385.

Emmerich, H., and M. Korn, 1987, Incorporation of attenuation into time-domain computations of seismic wave fields: Geophysics, **52**, 1252–1264.

Fraiser, C. W., 1970, Discrete-time solution of plane P-SV waves in a plane layered medium: Geophysics, **35**, 197–219.

Futterman, W. I., 1962, Dispersive body waves: Journal of Geophysical Research, **67**, 5279–5291.

Graves, R. W., 1996, Simulating seismic wave propagation in 3D elastic media using staggered-grid finite differences: Bulletin of the Seismological Society of America, **86**, 1091–1106.

Hestholm, S., 2002, Composite memory variable velocity-stress viscoelastic modelling: Geophysical Journal International, **148**, 153–162.

Kennett, B. L. N., 2001, The seismic wavefield, vol. I: Cambridge University Press.

Kinoshita, S., and M. Ohike, 2002, Attenuation characteristics of *S* waves in a sedimentary layer-basement system in the Kanto region, Japan: Zisin (Journal of The Seismological Society of Japan), **55**, 19–31 (in Japanese with English abstract).

Klimentos, T., 1995, Attenuation of P- and S-waves as a method of distinguishing gas and condensate from oil and water: Geophysics, **60**, 447–458.

Kormendi, F., and M. Dietrich, 1991, Nonlinear waveform inversion of plane-wave seismograms in stratified elastic media: Geophysics, **56**, 664–674.

Levander, A., 1988, Fourth-order finite difference P-SV seismograms: Geophysics, **53**, 1425–1436.

Liu, F., D. N. Whitmore, D. W. Hanson, R. S. Day, and C. C. Mosher, 2004, The impact of reciprocity on prestack source plane wave migration: 74th Annual International Meeting, SEG, Expanded Abstracts, 1045–1048.

Liu, H. P., D. L. Anderson, and H. Kanamori, 1976, Velocity dispersion due to anelasticity; Implications for seismology and mantle composition: Geophysical Journal of the Royal Astronomical Society, **47**, 41–58.

McCowan, D. W., and H. Brysk, 1989, Cartesian and cylindrical slant stacks, *in* P. L. Stoffa, ed., Tau-P: A plane-wave approach to the analysis of seismic data, Kluwer, 1–33.

Moczo, P., E. Bystricky, J. Kristek, J. M. Carcione, and M. Bouchon, 1997, Hybrid modeling of P-SV seismic motion at inhomogeneous viscoelastic topographic structures: Bulletin of the Seismological Society of America, **87**, 1305–1323.

Moczo, P., and J. Kristek, 2005, On the rheological models used for time-domain method of seismic wave propagation: Geophysical Research Letters, **32**, 1306; http://dx.doi.org/10.1029/2004GL021598.

Moczo, P., J. Kristek, V. Vavycuk, R. J. Archuleta, and L. Halda, 2002, 3D heterogeneous staggered-grid finite difference modeling of seismic motion with volume harmonic and arithmetic averaging of elastic moduli and densities: Bulletin of the Seismological Society of America, **92**, 3042–3066.

Mosher, C. C., T. H. Keho, A. B. Weglein, and D. J. Foster, 1996, The impact of migration on AVO: Geophysics, **61**, 1603–1615.

Müller, G., 1971, Direct inversion of seismic observations: Journal of Geophysics, **37**, 225–235.

O'Connell, R. J., and B. Budiansky, 1978, Measures of dissipation in viscoelastic media: Geophysical Research Letters, **5**, 5–8.

Pai, D. M., 1988, Generalized *f-k* (frequency-wavenumber) migration in arbitrarily varying media: Geophysics, **53**, 1547–1555.

Robertsson, J. O. A., 1996, A numerical free-surface condition for elastic/viscoelastic finite-difference modeling in the presence of topography: Geophysics, **61**, 1921–1934.

Robertsson, J. O., J. O. Blanch, and W. W. Symes, 1994, Viscoelastic finite-difference modeling: Geophysics, **59**, 1444–1456.

Shan, G., and B. Biondi, 2004, Imaging overturned waves by plane-wave migration in tilted coordinates: 74th Annual International Meeting, SEG, Expanded Abstracts, 969–972.

Stork, A. L., and H. Ito, 2004, Source parameter scaling for small earthquakes observed at the western Nagano 800-m-deep borehole, central Japan: Bulletin of the Seismological Society of America, **94**, 1781–1794.

Suzuki, H., R. Ikeda, T. Mikoshiba, S. Kinoshita, H. Sato, and H. Takahashi, 1981, Deep well-logs in Kanto-Tokai area: Review of Research for Disaster Prevention, **65**, 1–162 (in Japanese with English abstract).

Tanaka, H., and H. Takenaka, 2005, An efficient FDTD solution for plane-wave response of vertically heterogeneous media: Zisin (Journal of the Seismological Society of Japan), **57**, 343–354 (in Japanese with English abstract).

Treitel, S., P. R. Gutowski, and D. E. Wagner, 1982, Plane-wave decomposition of seismograms: Geophysics, **47**, 1375–1401.

Tygel, M., and P. Hubral, 1985, Transient plane-wave transforms for the point-source seismogram: Geophysics, **50**, 2889–2891.

Ursin, B., and A. Stovas, 2002, Reflection and transmission response of a layered isotropic viscoelastic medium: Geophysics, **67**, 307–323.

Virieux, J., 1984, SH-wave propagation in heterogeneous media: Velocity-stress finite-difference method: Geophysics, **49**, 1933–1957.

———, 1986, P-SV wave propagation in heterogeneous media: Velocity-stress finite-difference method: Geophysics, **51**, 889–901.

Yamamizu, F., H. Takahashi, N. Goto, and Y. Ohta, 1981, Shear wave velocities in deep soil deposits, part III: Zisin (Journal of the Seismological Society of Japan), **34**, 465–479 (in Japanese with English abstract).

Errata

To: **"Efficient FDTD algorithm for plane-wave simulation for vertically heterogeneous attenuative media,"** *Arash Jafar-Gandomi and Hiroshi Takenaka*, GEOPHYSICS, **72**, no. 4, H43–H53.

The peer-reviewed code related to this article was listed incorrectly. We apologize for any inconvenience caused by this error.

Following is a link to the correct code: http://software.seg.org/2007/0005.

To: **"CRP-based seismic migration velocity analysis,"** *Weihong Fei and George A. McMechan*, GEOPHYSICS, **71**, no. 3, U21–U28.

Equations 3 and 4 were printed incorrectly. We apologize for any inconvenience caused by this error.

The correct equations are:

$$T' = [T_{cal} + \frac{2\Delta l \cos(\theta_{cal})}{V_{old,r}}] * \alpha, \tag{3}$$

and

$$\Delta V_{new} = \frac{V_{old}}{\alpha} - V_{old}. \tag{4}$$